Materials Horizons

ROYAL SOCIETY OF CHEMISTRY

COMMUNICATION

View Article Online
View Journal | View Issue

Check for updates

Cite this: *Mater. Horiz.*, 2022, 9, 3031

Received 3rd June 2022,
Accepted 12th September 2022

DOI: 10.1039/d2mh00693f

rsc.li/materials-horizons

Multi-target cell therapy using a magnetoelectric microscale biorobot for targeted delivery and selective differentiation of SH-SY5Y cells *via* magnetically driven cell stamping†

Hyunseok Song,[ab] Dong-in Kim,[ab] Sarmad Ahmad Abbasi,[ab] Nader Latifi Gharamaleki,[ab] Eunhee Kim,[c] Chaewon Jin,[d] Samhwan Kim,[e] Junsun Hwang,[ab] Jin-Young Kim,[bc] Xiang-Zhong Chen,[f] Bradley J. Nelson,[f] Salvador Pané *[f] and Hongsoo Choi*[abg]

Cell therapy refers to a treatment that involves the delivery of cells or cellular material by means of injection, grafting, or implantation in order to replace damaged tissue and restore its function, or to aid the body in fighting disease. However, limitations include poor targeting delivery and low therapeutic efficacy due to low cell survival. Hence, novel approaches are required to increase cell delivery efficiency and enhance therapeutic efficacy *via* selective cell differentiation at target areas. Here, we present a stamping magnetoelectric microscale biorobot (SMMB) consisting of neuron-like cell spheroids loaded with magnetoelectric nanoparticles. The SMMB enables not only effective targeted delivery of cells to multiple target areas (*via* minimally invasive stamping employing magnetic actuation) but also facilitates selective neuronal differentiation *via* magnetoelectric (ME) stimulation. This ensures rapid colonization and enhances efficacy. SMMBs were fabricated using SH-SY5Y cells. Magnetoelectric nanoparticles for ME stimulation responded to an alternating magnetic field that ensured targeted cell differentiation. Multi-target cell therapy facilitated the targeted delivery and selective differentiation of SH-SY5Y cells to multiple regions using a single SMMB with rotating and alternating magnetic fields for delivery and ME stimulation. This promising tool may overcome the limitations of existing cell therapy for neurodegenerative diseases.

New concepts

Cell therapies suffer from several drawbacks including invasiveness, low delivery efficiency, induction of tissue trauma, or graft rejection. While efforts have been made to realize minimally invasive approaches for cell therapy, the therapeutic efficacy remains low. Here, we propose a minimally invasive approach for multi-target cell therapy using a highly integrated magnetoelectric biorobot. The device comprises a spheroidal functional chassis made of progenitor neuronal cells SH-SY5Y loaded with multiferroic magnetoelectric core–shell nanoarchitectures. The magnetoelectric biorobot not only enables precise cell transportation and delivery to multiple target areas *via* magnetically assisted stamping but also allows for wireless magnetoelectric electrostimulation and differentiation of cells after their deployment. This novel approach not only enables cell delivery for different target tissues and diseases but also allows for incorporating other multifunctional bioactive nanoarchitectures.

Introduction

Over the past 30 years, deaths and disability-adjusted life-years caused by degenerative neurological diseases, including Huntington's, Alzheimer's, Parkinson's diseases, and multiple sclerosis, have risen by 39% and 15%, respectively, as societies age.[1] Damage to neuronal tissues caused by neurological diseases is accompanied by degenerative dopaminergic neuron loss.[2] Because of this limited ability of regeneration, current treatments to address diseases of the central nervous system are not sufficient.

Cell therapies are a set of emerging treatments in biotechnology aimed at curing diseases by delivering cells to specific tissues. The aim of these therapies is diverse, spanning from

[a] *Department of Robotics and Mechatronics Engineering, Daegu Gyeongbuk Institute of Science and Technology (DGIST), Daegu, Republic of Korea. E-mail: mems@dgist.ac.kr*
[b] *DGIST-ETH Microrobotics Research Center, Daegu Gyeongbuk Institute of Science and Technology (DGIST), Daegu, Republic of Korea*
[c] *IMsystem Co., Ltd., Daegu, Republic of Korea*
[d] *Department of Division of Biotechnology, Daegu Gyeongbuk Institute of Science and Technology (DGIST), Daegu, Republic of Korea*
[e] *Brain Science Department, Daegu Gyeongbuk Institute of Science and Technology (DGIST) 711-873, Daegu, South Korea*
[f] *Institute of Robotics and Intelligent Systems, ETH Zurich, Zurich, CH-8092, Switzerland. E-mail: vidalp@ethz.ch*
[g] *Robotics Research Center, DGIST, Daegu, Republic of Korea*

† Electronic supplementary information (ESI) available. See DOI: https://doi.org/10.1039/d2mh00693f

tissue regeneration, restoration of biological function to the enhancement of the body's own means to fight disease.[3,4] Contrary to several drugs and biological formulations, delivered cells could cross biological barriers, react and adapt to biological cues and target specific cells, tissues or organs. Additionally, cells can be genetically engineered[5] or hitchhiked[6] to perform further therapeutic tasks. Recently, cell therapy using different types of cells (*e.g.*: neuronal stem cells (NSCs), neuronal progenitor cells) have shown promising outcomes *in vivo*. Depending on the delivered cell type, various effects can be attained including enhanced neurogenesis and neuroprotection, proliferation, immunomodulation, or immunosuppression. For example, the delivery of NSCs promotes repair of the central nervous system (CNS) by enhancing neuroprotective effects and replacing diseased tissue with regenerated neural tissue, resulting in functional neurological recovery.[7–12] However, current approaches for cell therapies involving transplantation are invasive,[13,14] associated with a low delivery efficiency[15–19] and infliction of direct tissue trauma,[20,21] and may be associated with graft rejection caused by immunological activation.[22,23]

While the safety and efficacy of cell therapies are improved by the use of minimally invasive targeted cell delivery, therapeutic efficacy remains unacceptable given the low cell survival rates ($\sim$5%) and unreliable differentiation into targeted cells *in vivo*.[24–28] For example, selective colonization by NSCs that differentiate only after arrival at a target area resolves these issues.[29,30] Neurotrophins, including nerve growth factor (NGF), generally serve as chemical stimuli.[31,32] However, NGF is inefficient *in vivo* because of the rapid diffusion rate, difficulties with delivery, and short half-life.[33,34] Such limitations may be solved by directly stimulating cells to initiate neuronal differentiation at a certain time after complete delivery.[35–39] Various external sources, including light,[40] magnetic fields,[41] and sound waves,[37] have been used to induce or enhance targeted neuronal differentiation. Of these, only magnetic fields allow for deep-tissue access (with little or no attenuation) given the low magnetic susceptibility of biological materials.[42]

Increasing the effective cell counts in the target areas is essential to enhance the therapeutic efficiency of stem cell therapies such as NSCs and reduce the side effects associated with repeated treatments.[25,28] This requires the search for effective cell delivery methods up to the point of transplantation and methods of genetic control such as the targeted differentiation of stem cells. One of the cell delivery methods that increase treatment efficiency is to make cells in the form of small magnetic robots and use magnetic fields to mobilize and deliver them to the target area. Suppose genetic control such as cell differentiation by cell stimulation with another kind of magnetic field is carried out at the same time. In that case, it might be possible to shorten the treatment time and improve the treatment effect.

Recently, multiferroic magnetoelectric nanomaterials actuated by external alternating magnetic fields have been proposed as transducers for electrically driven cell stimulation and differentiation. These nanomaterials consist of intimate combinations of piezoelectric and magnetostrictive components, usually in the form of core–shell nanoarchitectures. When exposed to alternating magnetic fields, magnetostrictive parts experience a change in their volume, thus transferring stress to the piezoelectric component, which is ultimately electrically polarized. This wireless generation of electric fields using magnetoelectric (ME) nanoparticles (MENPs) has been recently exploited for biomedical applications in cell stimulation and differentiation.[43–46] Furthermore, as MENPs also exhibit ferromagnetic behavior, they can also serve as motility components for small-scale robotic platforms.[17]

Considering current challenges in cell therapy and the potential advantages of motile small-scale robots and magnetoelectric nanomaterials, here we propose a stamping magnetoelectric microscale biorobot (SMMB) made of SH-SY5Y neuroblastoma cell spheroids loaded with MENPs. The SMMB moves in the desired direction to the desired area (target) *via* a process controlled by a magnetic field. Cell stamping (the release of SH-SY5Y cells and MENPs from the SMMB) occurs when the SMMB pauses (*i.e.*, the magnetic field controlling motion is switched off); cells are then delivered to multiple targets. ME stimulation of the MENPs causes the SH-SY5Y cells to differentiate; the cells are differentiated on the targets when an alternating magnetic field (AMF) is applied. The MENPs consist of cobalt ferrite (CFO) cores wrapped by piezoelectric barium titanate (BTO) shells using a sol–gel method.[47] We selected SH-SY5Y cells as they are widely used as a model for neurodegenerative disorders and differentiation studies. ME coupling of MENPs was observed *via* piezoresponse force microscopy (PFM) under an external magnetic field.[48–51] The MENPs were co-cultured with SH-SY5Y cells to form SMMBs for cell delivery and ME stimulation. The MENP load in the biorobots was chosen after biocompatibility considerations. SMMB movement was induced using a rotating magnetic field (RMF) after magnetizing the MENPs of the SMMBs. To demonstrate the multi-target cell abilities using a single SMMB, the SMMB was directed to multiple target areas, and SH-SY5Y cell proliferation was then induced *via* stamping. ME stimulation, generated by activating the MENPs *via* an AMF, triggered the differentiation of proliferated SH-SY5Y cells. Cell differentiation was quantified by measuring the levels of a neuronal differentiation marker *via* immunofluorescence staining. Our SMMB for multi-targeted therapy ensures selective neuronal differentiation after delivery of SH-SY5Y cells to a target region. This enhances therapeutic efficacy when treating neurodegenerative diseases and overcomes the limitations of existing stem cell therapy.

Results and discussion

Preparation and characterization of $CoFe_2O_4$@$BaTiO_3$ core–shell MENPs

The MENPs were prepared with cobalt ferrite ($CoFe_2O_4$, CFO) nanoparticles (the magnetostrictive core) and barium titanate ($BaTiO_3$, BTO) (the piezoelectric shell) to drive the SMMBs

magnetically and allow neuronal ME stimulation (Fig. S1 in the ESI†). MENPs were prepared by coating commercially available CFO cores with crystalline BTO shells employing a sol–gel method followed by thermal annealing. First, a citric acid solution containing $BaCO_3$ and $Ti(OCH(CH_3)_2)_4$, which served as sources of Ba and Ti, respectively, were prepared. Next, CFO nanoparticles were added in this solution. Gelation around the cores was induced by partial drying; BTO shells formed on the CFO cores. Finally, thermal annealing was used to obtain core–shell nanoarchitectures of CFO@BTO. The morphology of the MENPs was characterized *via* transmission electron microscopy (TEM), (Fig. 1a), which revealed core–shell structures, with the darker and lighter regions corresponding to the CFO cores (green dashes in the magnified image) and the surrounding BTO shells (yellow dashes in the magnified image), respectively. The energy-dispersive X-ray (EDX) maps show the elementary distribution throughout the MENP nanostructure (Fig. 1b). Uniform BTO shells enclose CFO cores. The phase purity and crystalline structure of the MENPs were evaluated by X-ray diffraction (XRD) (Fig. 1c). The observed XRD patterns can be assigned to two different reflections of the ferrite CFO phase of the $Fd\bar{3}m$ space group (ICDD:98-016-7445) and the ferroelectric BTO phase of the $P4mm$ space group (ICDD:98-001-5453). No trace of any impurity or an intermediate phase was evident.

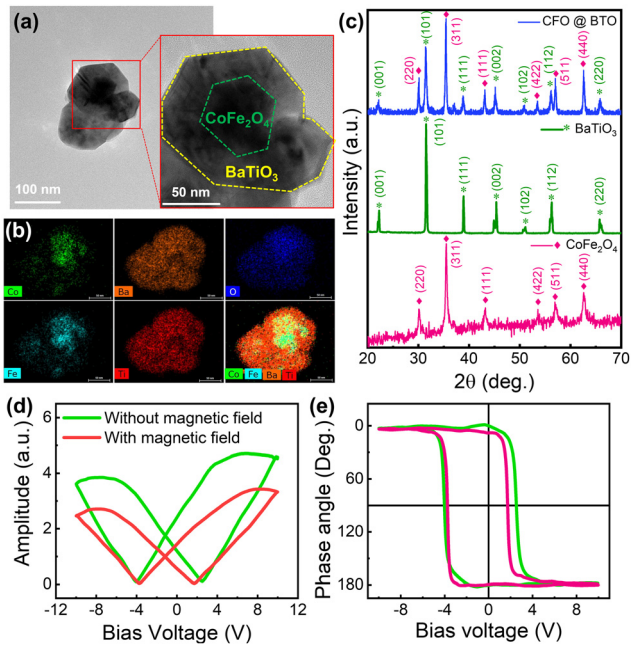

Fig. 1 Characterization of core–shell $CoFe_2O_4$@$BaTiO_3$ MENPs prepared by the sol–gel method. (a) Transmission electron microscopy (TEM) image of the CFO@BTO nanoparticles showing a clear core–shell structure. (b) EDX mapping images of MENPs highlighting the presence of a BTO shell over the CFO core as revealed by the elemental distributions of Co and Fe in the CFO core and Ba and Ti in the BTO shell. (c) X-Ray diffraction patterns of the MENPs, BTO, and CFO (*: BTO phase, ♦: CFO phase). (d) Local piezoresponse, amplitude voltage butterfly loops, and (e) phase voltage hysteresis loops of the MENPs during ferroelectric and magnetoelectric characterization using PFM with and without a magnetic field of 1 kOe.

The magnetic properties of pure CFO and CFO@BTO MENPs were characterized by vibrating sample magnetometry (VSM). Fig. S2 (ESI†) shows the magnetic hysteresis loops, which reveal a ferromagnetic behavior for both CFO and CFO@BTO nanoparticles. The saturation magnetizations (M_s values) for CFO and MENPs were 52 and 28 emu g^{-1}, respectively. The lower value for MENPs compared to CFO was due to the incorporation of the non-magnetic BTO shells on the CFO cores.

The ferroelectricity and magnetoelectricity (ME) of a single CFO@BTO MENP were investigated by comparing the PFM results with and without the application of an externally applied magnetic field. A DC bias voltage was applied to switch the direction of MENP polarization during PFM measurement. The corresponding piezoresponse hysteresis loops, namely, the butterfly loops (amplitude *vs.* bias voltage) and hysteresis loops (phase angle *vs.* bias voltage), are illustrated in Fig. 1d and e. Fig. 1e shows that the phase angles are switched between 0° and 180° with or without an external magnetic field, indicating that in both cases, the measured signals are piezoelectric rather than electrostatic responses. The results also show that the nanoparticles exhibit ferroelectricity, and that the strain generated by the magnetostrictive phase is efficiently transferred to the piezoelectric phase. The horizontal shifts of the piezoresponse phase loops and the asymmetrical butterfly shapes of the amplitude curves may be caused by work function differences between the conductive cantilever tip and the MENPs. When the external magnetic field was removed, the corresponding coercive voltages for the piezoelectric BTO shell were −4.04 and 2.49 V, respectively. Under an external magnetic field of 1 kOe, the coercive voltages shifted to −3.75 and 1.73 V, respectively. The shifts of the coercive voltage (0.29 V positive and 0.76 V negative) upon application of the magnetic field evidence effective transmission of strain caused by the magnetostrictive CFO core followed by MENP magnetoelectricity. Note that the asymmetric coercive voltage offsets of the piezoresponse loops can be used to estimate the ME coefficients. The direct ME coupling coefficient (α_{ME}), which reflects coupling between the piezoelectric (p) and magnetostrictive (λ) phases, is:[52,53]

$$\alpha_{ME} = p \times \lambda = \frac{\Delta E}{\Delta S} \times \frac{\Delta S}{\Delta H} = \frac{\Delta E}{\Delta H} = \frac{\Delta V/t}{\Delta H} \left(\mathrm{V\ cm^{-1}\ Oe^{-1}}\right)$$

where ΔE, ΔS, and ΔH are the electric field, the strain, and the magnetic field change, respectively. The electric field is defined as the voltage change (ΔV) divided by the thickness (t) of the piezoelectric material. The equation yields a local ME coupling coefficient for the CFO@BTO MENPs used hereof (0.76–0.29 V)/(2 × 50 nm × 1 kOe) = 47 V cm^{-1} Oe^{-1}. This value is at the same order of magnitude as those of previously reported one-dimensional core–shell magnetoelectric nanostructures.[48–51]

Fabrication of the SMMB composed of MENPs and SH-SY5Y cells

Fig. 2a shows a schematic of SMMB fabrication *via* aggregation of MENPs and SH-SY5Y cells in a U-bottomed 96-well plate (more details can be found in the experimental section of the

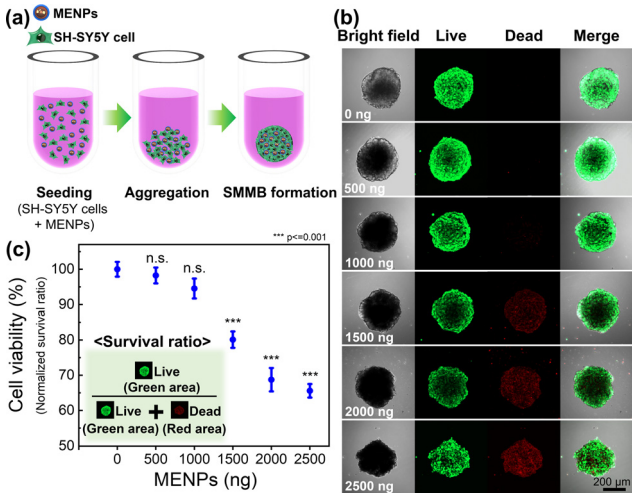

Fig. 2 (a) Schematic of spheroid assembly using MENPs during fabrication of SMMBs in U-bottomed 96-well plates. (b) Fluorescent live/dead cell analysis of SMMBs with various numbers of particles (0–2500 ng) (green: live; red: dead) and (c) survival ratio by particle number. Survival ratio = green area/(green area + red area).

ESI†). To assess at which concentrations MENPs can become cytotoxic, the MENP loading was varied from 0 to 2500 ng per spheroid to optimize the MENP/spheroid ratio, and biocompatibility was then investigated *via* live/dead staining (Fig. 2b). Biocompatibility was quantified by normalizing the survival ratio [live cell area (green) to the total cell area (green plus red)] (Fig. 2c). SMMBs with <1000 ng MENPs/spheroid exhibited good viability ($>90\%$ of the control); SMMBs with higher concentrations of MENPs (>1500 ng per spheroid) evidenced significant decreases in cell viability, possibly because the physical barrier imposed by high concentrations of MENPs induced hypoxia. The sizes of the SMMBs were measured as a function of MENP loading (from 0 to 2500 ng) (Fig. S3, ESI†). SMMBs with low MENPs contained (≤ 1000 ng) were slightly smaller than those with higher loading, and their cells were stable and well-packed. SMMBs with loading higher than 1500 ng MENPs were larger because cell compactness was reduced by the MENP barriers. Additionally, disaggregation of cells from SMMBs evidenced the toxic effects of higher MENP concentrations. To maximize SMMB locomotion and ME stimulation while preserving the stability of the cell spheroid, we chose to work with spheroids loaded with 1000 ng of MENP.[54] Fig. S4 (ESI†) shows the surfaces of SMMBs with and without MENPs. The red dots in the lower left image show well-distributed MENPs in SMMBs. Morphological analysis of SMMB cross-sections (TEM images) revealed the distribution of MENP distribution through the aggregated SH-SY5Y cells (Fig. S5, ESI†).

Targeted locomotion of the SMMB

The locomotion of SMMBs under a rotating magnetic field (RMF) generated by an eight-coil electromagnetic system was evaluated *in vitro*. RMF was used because spherical micromotors are thus efficiently driven, given the force difference caused by the hydrodynamic mismatch between the top and bottom of the motor.[55,56] An SMMB was immersed in phosphate-buffered saline (PBS) and set in the working space of the electromagnetic system (Fig. S6, ESI†). Fig. 3a shows the targeted locomotion caused by the magnetic torque exerted on the CFO core upon an RMF application (15 mT at 5 Hz). The SMMB was manually controlled from the start point (0 s), followed a crown-shaped path, and returned to the start point after 80 s (Video S1, ESI†). The RMF direction changed at 13, 20, 29, 36, 46, and 56 s. The SMMB followed the rapidly changing external RMF without any delay. It is thus possible to accurately position the SMMB in a fluid using an external magnetic field. The linear translational velocities of the SMMB were measured as a function of rotation frequency from 1 to 39 Hz (Fig. 3b), as the RMF intensity varied from 5 to 20 mT. At all RMF intensities, the velocity increased almost linearly with the increase in RMF frequency until attainment of the step-out frequencies (determined by the RMF intensities). Above these frequencies, the velocities decreased drastically as the RMF rotation was too high to enable a synchronous SMMB rotation.[57,58] The step-out frequencies were 17 Hz at 5 mT, 21 Hz at 10 mT, 29 Hz at 15 mT, and 31 Hz at 20 mT; the respective maximum velocities were 1.0, 1.3, 1.4, and 1.6 mm s^{-1}. Thus, the step-out threshold improved with an increase in magnetic field intensity, which in turn increased the maximum achievable velocity. The cell viability in the SMMB before and after magnetic manipulation is shown in Fig. S7 (ESI†). The adenosine triphosphate (ATP) levels of cells in the SMMB decreased negligibly after manipulation in comparison to cells in SMMB prior to manipulation, revealing that cell loss/reduced viability was minimal during magnetic manipulation.

The principal advantage of targeted cell delivery is that minimally invasive and accurate local site targeting is possible while side effects are reduced. The disadvantages are the need for repeated procedures and significant cell losses prior to target attainment (for several reasons, including an immune response).[13,14] These disadvantages can be partially overcome if multiple treatments are delivered over a wide area by spreading cells from a single dose of biorobots. Therefore, we performed a multi-target cell therapy (using a stamping method *in vitro*) to confirm that it was possible to maximize the treatment efficacy *via* a single procedure (Fig. 4a). When an SMMB is seeded on a target for a certain period of time, the SH-SY5Y cells from the

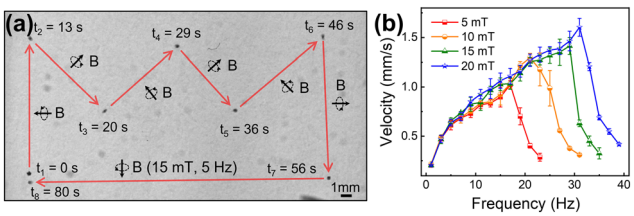

Fig. 3 (a) A time-lapse image of magnetic rolling SMMB locomotion under an external rotating magnetic field (RMF) of 15 mT at 5 Hz. (b) Translational velocities of the SMMBs at various RMF intensities from 5 to 20 mT and rotating frequencies of 1 to 39 Hz. (maximum velocity 1.6 mm s^{-1} at 31 Hz and 20 mT).

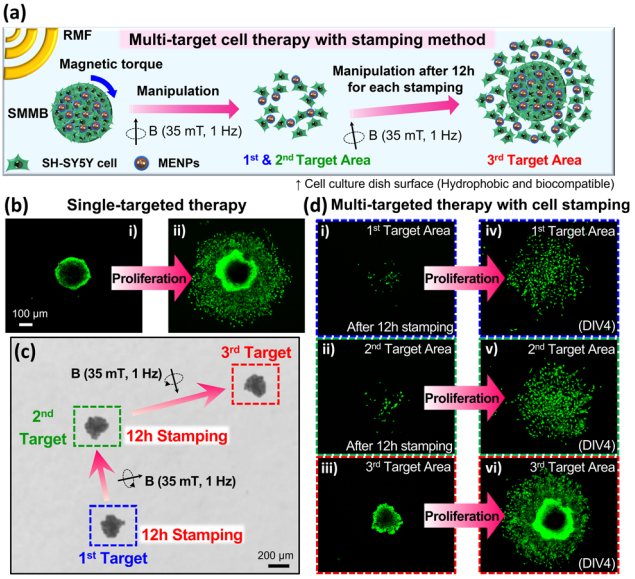

Fig. 4 (a) Schematic of multi-targeted cell therapy achieved by moving SMMBs from 1st target to 2nd and 3rd targets ('stamping'). (b) Fluorescence images of single-targeted therapy as revealed by a cell tracker. (i) The SMMB remaining on the single target and (ii) cells that proliferated over 4 days on the single target. (c) The SMMB was moved to the first target by the RMF (35 mT, 1 Hz) and held there for 12 h (for stamping); the SMMB was then delivered to the second target (again by the RMF) and, after 12 h of stamping, moved to the third target. (d) Fluorescence images of multi-targeted therapy as revealed by a cell tracker. Cells remain on (i) the 1st and (ii) the 2nd targets. In (iii), the SMMB has moved to the 3rd target after stamping the 1st and 2nd targets for 12 h each. Cells that proliferated on the (iv) 1st, (v) 2nd, and (vi) 3rd targets 4 days after the first SMMB seeding (the 1st target).

SMMB spread out in the culture dish. Fig. 4b shows the results of single-target therapy. The SMMB was seeded and cultured for 4 days, and the cells proliferated on the target. Fig. 4c shows a multi-target therapy (one SMMB, three targets, and two stampings). The SMMB remained on the first and second targets for 12 h; SH-SY5Y cells were then released. The RMF moved the SMMB from the first to the second target, and then from the second to the third target. When an SMMB is held in the same place in a culture dish for a long time, the SMMB binds to the dish and is not moved by a strong, external magnetic field. Thus, the SMMBs were held on targets for only 12 h. The stamped cells were stained with a tracker prior to seeding into the culture dish (to allow measurement of cell proliferation at each target). The cells released at the first (Fig. 4d(i)), second (Fig. 4d(ii)), and third targets (Fig. 4d(iii)) were cultured for 4 days, during which the cell areas increased (Fig. 4d(iv–vi)). Cell numbers were compared by quantifying the ATP levels (Fig. S8, ESI†). Cell proliferation after multi-target therapies (two or three targets) was 37% and 68% higher than after single-target therapy.

Differentiation of SH-SY5Y cells by ME stimulation

Fig. 5a schematically shows the selective differentiation of SH-SY5Y cells induced by ME stimulation when the MENPs are under an external AMF. The detailed procedure is shown in Fig. S9 (ESI†). An electromagnetic coil was placed directly over the SMMB-seeded cell culture dish to initiate selective cell differentiation triggered by the AFM (Fig. S10, ESI†). As the cells proliferated and spread from the SMMB on the dish during ME stimulation, the MENPs migrated with the cells (Fig. S11a, ESI†), remaining evenly distributed over the entire area and in contact with cells (Fig. S11b–d, ESI†). Thus, almost all cells can be magnetoelectrically stimulated. Before ME stimulation, the cells in the SMMB were stained with a cell tracker to enable morphological observation of proliferating live cells. An AMF (30 mT at 30 Hz) was applied to the cells for 30 min per day. We formed four experimental groups that differed in terms of the presence/absence of MENPs and AMF. We verified that neuronal differentiation was selectively triggered by ME stimulation of MENPs by the external AMF. Fig. 5b shows the green area of live cells after 7 days of ME stimulation. The magnetoelectrically stimulated group (thus with MENPs and AMF; +AMF/+MENPs) of Fig. 5b(iv) exhibits a significantly narrower cellular area than do the other three

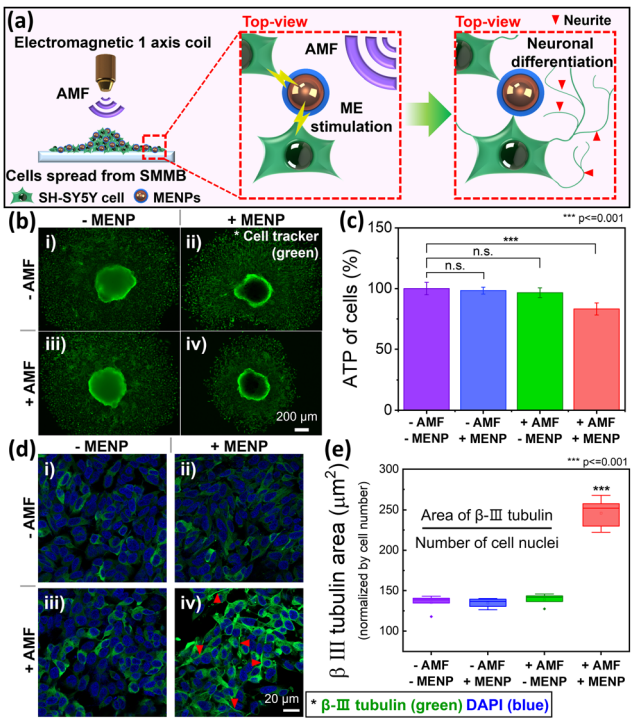

Fig. 5 (a) Neuronal differentiation of SH-SY5Y cells seeded from SMMBs *via* magnetoelectric stimulation; the MENPs are activated by an external AMF. (b) Neuronal differentiation *via* ME stimulation under four experimental conditions (with and without MENPs) as revealed by AFM. The morphologies of SMMBs settled on cell cultures were measured after 7 days of ME stimulation to verify differentiation. The cells were stained with a cell tracker prior to seeding to reveal them clearly. (c) The cell amount under each condition (obtained *via* ATP measurements). (d) Immunofluorescence images of β-III tubulin (green) and DAPI (blue) to verify cell differentiation *via* ME stimulation. Neurites are marked with red arrows. (e) The β-III tubulin-positive cell areas (normalized by nuclear number) were used to compare quantitatively the cell differentiation levels (*** $p \leq 0.001$).

groups [Fig. 5b (i): −AMF/−MENPs, (ii): −AMF/+MENPs, and (iii): +AMF/−MENPs]. The narrow cell area of Fig. 5b(iv) reflects reduced MENP-stimulated cell proliferation. We measured ATP levels (on day 7) to quantify the amount of proliferated cells (Fig. 5c) and compared the values to that of the control group. The +AMF/+MENPs group [Fig. 5b(iv)] evidenced a significantly lower ATP level (by 23%) than the control group. In comparison, the other two groups [Fig. 5b(ii and iii)] evidenced negligible differences ($\leq$4%) from the control group [Fig. 5b(i)]. As cell proliferation slows during neuronal differentiation, the reduced proliferation of SH-SY5Y cells in the +AMF/+MENP group indicates that ME stimulation triggered the differentiation.[59–61]

Immunofluorescence assays of protein biomarkers are widely used to explore neuronal differentiation. We employed β-III tubulin as a marker of SH-SY5Y neuronal cell differentiation.[35,61] Fig. 5d shows the SH-SY5Y cell immunofluorescence images of the groups of Fig. 5b. The areas of immunofluorescence measurement (including cells and MENPs that spread from the SMMBs) were randomly selected in all dishes. The typical neuronal marker β-III tubulin was expressed in green and DAPI for nuclei in blue. Qualitatively, neurite outgrowth was evident in only the +AMF/+MENPs group [red arrows in Fig. 5d(iv)]. The other groups [Fig. 5d(i–iii)] evidenced no significant morphological alterations because the SH-SY5Y cells did not undergo ME stimulation. To quantify neuronal differentiation of SH-SY5Y cells induced by ME stimulation, the β-III tubulin levels were estimated by measuring the green fluorescent area normalized by the number of nuclei (blue) (Fig. 5e).[62] ME stimulation enhanced the β-III tubulin level by 82% compared to that of undifferentiated SH-SY5Y cells lacking stimulation ($p \leq 0.001$). Thus, SH-SY5Y neuroblastoma cells from SMMBs successfully differentiated into neuron-like cells on ME stimulation generated by applying an AMF to the MENPs.

Conclusions

We used SMMBs to target cell delivery to multiple areas employing an external RMF and induced selective neuronal differentiation *via* ME stimulation by an AMF. The SMMBs were prepared by co-culturing MENPs and SH-SY5Y cells. MENPs were fabricated by coating magnetostrictive CFO cores with piezoelectric BTO shells *via* the sol–gel method. The concentration of MENPs in the SMMBs was optimized at 1000 ng per SMMB *via* cell viability assessment. The SMMBs were manipulated (in PBS) by an external RMF with a speed of up to 1.6 mm s^{-1}. A single SMMB delivered SH-SY5Y cells to more than one target area and may thus improve the efficacy of multi-target cell therapy. Neuronal differentiation induced by ME stimulation of MENPs by the AMF was confirmed by immunofluorescence staining of SH-SY5Y cells for the neuronal marker β-III tubulin. Given these results, our SMMBs may serve as an alternative to conventional neural stem cell therapy, improving therapeutic efficacy *via* multi-target cell delivery, increasing neural differentiation, and reducing side effects because the method is non-invasive. Increasing the amounts of proliferated cells by stamping multiple targets with SMMBs will improve cell survival and reduce the side effects of repeated *in vivo* therapies.

Author contributions

H. S. and H. C. conceived the concept and initiated the project; H. S., D. K, and S. K. prepared the samples; N. G. prepared experimental set-up; H. S. wrote the manuscript; H. S., E. K., C. J., J. H., and H. C. contributed to experimental characterization and data analysis; J. K., X. C., B. N., S. P., and H. C. supervised the research and discussed the results; D. K., S. A., S. P., and H. C. revised the manuscript; All the authors confirmed the final version of the manuscript.

Conflicts of interest

The authors declare no competing financial interest.

Acknowledgements

We are grateful to all the members of DGIST-ETH Microrobotics Research Center and Bio-microrobotics Lab for their sincere help and comment. We thank the Center for Core Research Facilities of DGIST. This work was financially supported by the National Convergence Research of Scientific Challenges and Global Research Laboratory through the National Foundation of Korea (NRF) and the DGIST R&D Program (No. 2021M3F7A1082275, No. 2017K1A1A2013237, No. 2017M3A9G8084463, and 21-CoE-BT-02) funded by the Ministry of Science and ICT. S. P. acknowledges support from the ERC-2017-CoG HINBOTS (Grant No. 771565) and the Swiss National Science Foundation (Project No. 200021L_192012).

Notes and references

1 V. L. Feigin, T. Vos, E. Nichols, M. O. Owolabi, W. M. Carroll, M. Dichgans, G. Deuschl, P. Parmar, M. Brainin and C. Murray, *Lancet Neurol.*, 2020, **19**, 255–265.
2 S. Majd, J. H. Power and H. J. M. Grantham, *BMC Neurosci.*, 2015, **16**, 69.
3 E. Thomas Pashuck and M. M. Stevens, *Sci. Transl. Med.*, 2012, **4**, 160sr4.
4 L. L. W. Wang, M. E. Janes, N. Kumbhojkar, N. Kapate, J. R. Clegg, S. Prakash, M. K. Heavey, Z. Zhao, A. C. Anselmo and S. Mitragotri, *Bioeng. Transl. Med.*, 2021, **6**, e10214.
5 S. B. Yong, J. Y. Chung, Y. Song and Y. H. Kim, *J. Pharm. Invest.*, 2018, **48**, 199–208.
6 J. S. Brenner, D. C. Pan, J. W. Myerson, O. A. Marcos-Contreras, C. H. Villa, P. Patel, H. Hekierski, S. Chatterjee, J. Q. Tao, H. Parhiz, K. Bhamidipati, T. G. Uhler, E. D. Hood, R. Y. Kiseleva, V. S. Shuvaev, T. Shuvaeva, M. Khoshnejad, I. Johnston, J. V. Gregory, J. Lahann, T. Wang, E. Cantu,

W. M. Armstead, S. Mitragotri and V. Muzykantov, *Nat. Commun.*, 2018, **9**, 2684.
7 S. Kelly, T. M. Bliss, A. K. Shah, G. H. Sun, M. Ma, W. C. Foo, J. Masel, M. A. Yenari, I. L. Weissman, N. Uchida, T. Palmer and G. K. Steinberg, *Proc. Natl. Acad. Sci. U. S. A.*, 2004, **101**, 11839–11844.
8 G. Martino, S. Pluchino, L. Bonfanti and M. Schwartz, *Physiol. Rev.*, 2011, **91**, 1281–1304.
9 A. V. Naumova, M. Modo, A. Moore, C. E. Murry and J. A. Frank, *Nat. Biotechnol.*, 2014, **32**, 804–818.
10 G. Martino and S. Pluchino, *Nat. Rev. Neurosci.*, 2006, **7**, 395–406.
11 S. Ge, E. L. K. Goh, K. A. Sailor, Y. Kitabatake, G. L. Ming and H. Song, *Nature*, 2006, **439**, 589–593.
12 O. Lindvall and Z. Kokaia, *J. Clin. Invest.*, 2010, **120**, 29–40.
13 X.-Z. Chen, J.-H. Liu, M. Dong, L. Müller, G. Chatzipirpiridis, C. Hu, A. Terzopoulou, H. Torlakcik, X. Wang, F. Mushtaq, J. Puigmartí-Luis, Q.-D. Shen, B. J. Nelson and S. Pané, *Mater. Horiz.*, 2019, **6**, 1512–1516.
14 O. Lindvall and Z. Kokaia, *Trends Pharmacol. Sci.*, 2009, **30**, 260–267.
15 R. S. Lappalainen, S. Narkilahti, T. Huhtala, T. Liimatainen, T. Suuronen, A. Närvänen, R. Suuronen, O. Hovatta and J. Jolkkonen, *Neurosci. Lett.*, 2008, **440**, 246–250.
16 W. Wang, K. Jin, X.-O. Mao, N. Close, D. A. Greenberg and Z.-G. Xiong, *Int. J. Clin. Exp. Med.*, 2008, **1**, 145–153.
17 J. Chen, P. R. Sanberg, Y. Li, L. Wang, M. Lu, A. E. Willing, J. Sanchez-Ramos and M. Chopp, *Stroke*, 2001, **32**, 2682–2688.
18 J. Baumgartner, P. K. Dash, D. Ph and C. S. Cox Jr., *J. Neurosurg.*, 2009, **110**, 1189–1197.
19 U. M. Fischer, M. T. Harting, F. Jimenez, W. O. Monzon-Posadas, H. Xue, S. I. Savitz, G. A. Laine and C. S. Cox, *Stem Cells Dev.*, 2009, **18**, 683–691.
20 B. A. Aguado, W. Mulyasasmita, J. Su, K. J. Lampe and S. C. Heilshorn, *Tissue Eng., Part A*, 2012, **18**, 806–815.
21 I. Caron, F. Rossi, S. Papa, R. Aloe, M. Sculco, E. Mauri, A. Sacchetti, E. Erba, N. Panini, V. Parazzi, M. Barilani, G. Forloni, G. Perale, L. Lazzari and P. Veglianese, *Biomaterials*, 2016, **75**, 135–147.
22 C. A. Herberts, M. S. G. Kwa and H. P. H. Hermsen, *J. Transl. Med.*, 2011, **9**, 1–14.
23 K. Sugaya and M. Vaidya, *Adv. Exp. Med. Biol.*, 2018, **1056**, 61–84.
24 S. Qiao, Y. Liu, F. Han, M. Guo, X. Hou, K. Ye, S. Deng, Y. Shen, Y. Zhao, H. Wei, B. Song, L. Yao and W. Tian, *Adv. Healthcare Mater.*, 2018, **7**, 1800080.
25 O. Lindvall, Z. Kokaia and A. Martinez-Serrano, *Nat. Med.*, 2004, **10**, S42–S50.
26 M. Ronaghi, S. Erceg, V. Moreno-Manzano and M. Stojkovic, *Stem Cells*, 2010, **28**, 93–99.
27 P. J. Hallett, M. Deleidi, A. Astradsson, G. A. Smith, O. Cooper, T. M. Osborn, M. Sundberg, M. A. Moore, E. Perez-Torres, A. L. Brownell, J. M. Schumacher, R. D. Spealman and O. Isacson, *Cell Stem Cell*, 2015, **16**, 269–274.
28 M. M. Adil, T. Vazin, B. Ananthanarayanan, G. M. C. Rodrigues, A. T. Rao, R. U. Kulkarni, E. W. Miller, S. Kumar and D. V. Schaffer, *Biomaterials*, 2017, **136**, 1–11.
29 T. Yasuhara, N. Matsukawa, K. Hara, G. Yu, L. Xu, M. Maki, S. U. Kim and C. V. Borlongan, *J. Neurosci.*, 2006, **26**, 12497–12511.
30 M. J. Cooke, K. Vulic and M. S. Shoichet, *Soft Matter*, 2010, **6**, 4988–4998.
31 R. Ferreira, J. Napoli, T. Enver, L. Bernardino and L. Ferreira, *Nat. Commun.*, 2020, **11**, 4265.
32 R. Levi-Montalcini, S. D. Skaper, R. Dal Toso, L. Petrelli and A. Leon, *Trends Neurosci.*, 1996, **19**, 514–520.
33 S. Zhang and H. Uludağ, *Pharm. Res.*, 2009, **26**, 1561–1580.
34 S. Tang, J. Zhu, Y. Xu, A. P. Xiang, M. H. Jiang and D. Quan, *Biomaterials*, 2013, **34**, 7086–7096.
35 G. G. Genchi, L. Ceseracciu, A. Marino, M. Labardi, S. Marras, F. Pignatelli, L. Bruschini, V. Mattoli and G. Ciofani, *Adv. Healthcare Mater.*, 2016, **5**, 1808–1820.
36 G. Ciofani, S. Danti, D. D'Alessandro, L. Ricotti, S. Moscato, G. Bertoni, A. Falqui, S. Berrettini, M. Petrini, V. Mattoli and A. Menciassi, *ACS Nano*, 2010, **4**, 6267–6277.
37 A. Marino, S. Arai, Y. Hou, E. Sinibaldi, M. Pellegrino and Y. Chang, *ACS Nano*, 2015, **9**, 7678–7689.
38 A. H. Rajabi, M. Jaffe and T. L. Arinzeh, *Acta Biomater.*, 2015, **24**, 12–23.
39 L. Liu, B. Chen, K. Liu, J. Gao, Y. Ye, Z. Wang, N. Qin, D. A. Wilson, Y. Tu and F. Peng, *Adv. Funct. Mater.*, 2020, **30**, 1910108.
40 A. Qu, M. Sun, J. Y. Kim, L. Xu, C. Hao, W. Ma, X. Wu, X. Liu, H. Kuang, N. A. Kotov and C. Xu, *Nat. Biomed. Eng.*, 2021, **5**, 103–113.
41 A. Tay, A. Kunze, C. Murray and D. Di Carlo, *ACS Nano*, 2016, **10**, 2331–2341.
42 R. Chen, A. Canales and P. Anikeeva, *Nat. Rev. Mater.*, 2017, **2**, 16093.
43 M. Nair, R. Guduru, P. Liang, J. Hong, V. Sagar and S. Khizroev, *Nat. Commun.*, 2013, **4**, 1707.
44 A. Chaudhuri and K. Mandal, *J. Magn. Magn. Mater.*, 2015, **377**, 441–445.
45 R. M. Thankachan, B. Raneesh, A. Mayeen, S. Karthika, S. Vivek, S. S. Nair, S. Thomas and N. Kalarikkal, *J. Alloys Compd.*, 2018, **731**, 288–296.
46 P. Kaviraj, R. Pramanik and A. Arockiarajan, *Ceram. Int.*, 2019, **45**, 12344–12352.
47 B. N. Rao, P. Kaviraj, S. R. Vaibavi, A. Kumar, S. K. Bajpai and A. Arockiarajan, *J. Appl. Phys.*, 2017, **122**, 164102.
48 F. Mushtaq, X. Chen, H. Torlakcik, C. Steuer, M. Hoop, E. C. Siringil, X. Marti, G. Limburg, P. Stipp, B. J. Nelson and S. Pané, *Adv. Mater.*, 2019, **1901378**, 1–8.
49 X. Z. Chen, M. Hoop, N. Shamsudhin, T. Huang, B. Özkale, Q. Li, E. Siringil, F. Mushtaq, L. Di Tizio, B. J. Nelson and S. Pané, *Adv. Mater.*, 2017, **29**, 1605458.
50 S. Xie, F. Ma, Y. Liu and J. Li, *Nanoscale*, 2011, **3**, 3152–3158.
51 A. Nicolenco, A. Gómez, X. Z. Chen, E. Menéndez, J. Fornell, S. Pané, E. Pellicer and J. Sort, *Appl. Mater. Today*, 2020, **19**, 100579.
52 H. Song, D. R. Patil, W. H. Yoon, K. H. Kim, C. Choi, J. H. Kim, G. T. Hwang, D. Y. Jeong and J. Ryu, *Energy Environ. Sci.*, 2020, **13**, 4238–4248.

53 H. Song, M. Peddigari, A. Kumar, S. Lee, D. Kim, N. Park, J. Li, D. R. Patil and J. Ryu, *J. Alloys Compd.*, 2020, **834**, 155124.
54 B. Wang, K. F. Chan, K. Yuan, Q. Wang, X. Xia, L. Yang, H. Ko, Y. X. J. Wang, J. J. Y. Sung, P. W. Y. Chiu and L. Zhang, *Sci. Rob.*, 2021, **6**, eabd2813.
55 S. Jeon, S. Kim, S. Ha, S. Lee, E. Kim, S. Y. Kim, S. H. Park, J. H. Jeon, S. W. Kim, C. Moon, B. J. Nelson, J. Young Kim, S. W. Yu and H. Choi, *Sci. Rob.*, 2019, **4**, eaav4317.
56 Y. Alapan, U. Bozuyuk, P. Erkoc, A. C. Karacakol and M. Sitti, *Sci. Rob.*, 2020, **5**, eaba5726.
57 D. C. J. Yang, J. M. Cai and Y. J. J. Yang, *Appl. Phys. Lett.*, 2018, **113**, 161901.
58 A. W. Mahoney, N. D. Nelson, K. E. Peyer, B. J. Nelson and J. J. Abbott, *Appl. Phys. Lett.*, 2014, **104**, 144101.
59 R. Giorgi Silveira, C. Perelló Ferrúa, C. C. do Amaral, T. Fernandez Garcia, K. B. de Souza and F. Nedel, *Brain Res. Bull.*, 2020, **157**, 140–148.
60 C. Zhao, G. Sun, S. Li and Y. Shi, *Nat. Struct. Mol. Biol.*, 2009, **16**, 365–371.
61 K. Murai, G. Sun, P. Ye, E. Tian, S. Yang, Q. Cui, G. Sun, D. Trinh, O. Sun, T. Hong, Z. Wen, M. Kalkum, A. D. Riggs, H. Song, G. L. Ming and Y. Shi, *Nat. Commun.*, 2016, **7**, 10965.
62 R. F. Simões, R. Ferrão, M. R. Silva, S. L. C. Pinho, L. Ferreira, P. J. Oliveira and T. Cunha-Oliveira, *Food Chem. Toxicol.*, 2021, **149**, 111967.

